The significance of gas release on the mixing of larger particles in bubbling fluidized beds

Fuel Processing Technology 291 (2026) 108542

Contents lists available at ScienceDirect

Fuel Processing Technology

journal homepage: www.elsevier.com/locate/fuproc

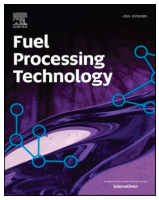

The significance of gas release on the mixing of larger particles in bubbling fluidized beds

Azka Rizwana Siddiqui [a,*], Jing Shi [a], Anna Köhler [b], Diana Carolina Guío-Pérez [a], David Pallarès [a]

[a] Division of Energy Technology, Department of Environmental and Energy Sciences,Chalmers University of Technology, SE-412 96 Gothenburg, Sweden
[b] BioShare AB, Karlstad, Sweden

ARTICLE INFO

Keywords:
Solids mixing
Solids segregation
Fluid-dynamic scaling
Stefan flow
Endogenous bubbles
Magnetic Particle Tracking

ABSTRACT

The mixing of larger particles (e.g., fuel particles) in a bubbling fluidized bed is governed by buoyancy and drag, which correspondingly promote segregation and internal circulation. Prior studies have shown that gas released from such particles during drying or devolatilization can generate so-called endogenous bubbles, which exert an effective lift force on the particle. However, the impact of gas release under bubbling conditions and with over-bed particle feeding, remains unexplored. This study investigates how gas release influences the mixing of such particles in a bubbling fluidized bed. Experiments were conducted in a fluid-dynamically downscaled model simulating biomass pyrolysis at 700 °C in a bed of silica sand fluidized with flue gas using magnetic particle tracking and gas-releasing tracers. Different behaviors were observed depending on the fluidization velocity. At low fluidization velocities ($u_0/u_{mf} \leq 2$), buoyant particles sink slightly deeper by locally reducing the concentration of surrounding suspension, whereas heavy particles experience inhibited sinking resulting in preferred positions closer to the bed surface. As fluidization velocity increases beyond $u_0/u_{mf} \geq 3.5$, the effect of gas release on axial mixing diminishes, while the lateral mixing becomes more pronounced, with the dispersion coefficient enhanced by up to 40%. These findings inform industrial fluidized-bed design.

1. Introduction

Fluidized beds are widely used at industrial scales due to their higher degree of gas-solid mixing, which results in superior interphase heat and mass transfer rates compared with other gas–solid contacting systems. These advantages have supported their extensive commercial application since the early 1940s in synthesis, thermochemical conversion, and various physical operations [1–4]. In many applications, fluidized beds contain more than one solid phase, each with distinct physical properties. While the fluidization of a single solid phase already produces a complex heterogenous system, the introduction of a secondary solids phase gives rise to additional interactions that can strongly influence the process performance. A homogenous solid distribution is often desirable to ensure effective contact between reactants, whereas controlled heterogenous distributions can be advantageous in processes aiming at narrow residence time distribution or solids separation [5,6]. Consequently, the mixing of solid phases becomes a key aspect of the process design that must be understood and controlled. In fact, previous studies have investigated the mixing behavior of the lean solids phase (e.g. fuel particles) relative to the bulk solids phase, providing valuable insights into the systems where such lean solids particles undergo thermal and/or chemical conversion [7–13]. These conversion systems involve industrially important fluidized-bed processes, in which the mixing of the lean solids phase relative to the bed material directly governs the process performance. Examples of this are: (i) in biomass fast pyrolysis and gasification, woody feedstocks (such as wood pellets, wood chips, torrefied biomass, or coarser residues) are continuously fed over a bed of silica sand or olivine, and their residence time and axial position in the bed govern the degree of devolatilization, and the char and tar yields [14–18]. (ii) In the pyrolysis of plastics (chemical recycling), denser polymer flakes such as PET tend to segregate axially and accumulate near the bottom of the fluidized bed, where their segregation and aggregation behavior is directly linked to local residence time, fluidization quality, and the risk of bed defluidization [19–21], which in turn can influence conversion and the resulting product quality. (iii) In catalytic and thermal pyrolysis of mixed-feedstock, fuel particles of one density

* Corresponding author.
E-mail address: azkar@chalmers.se (A.R. Siddiqui).

https://doi.org/10.1016/j.fuproc.2026.108542
Received 16 April 2026; Received in revised form 29 June 2026; Accepted 17 July 2026
Available online 30 July 2026

and size class come in contact with catalyst or bed-material particles of very different properties, and the relative mixing and segregation of these phases governs fuel–catalyst contact and thereby the conversion rates [22–24]. Underlying these examples is a complex interplay of particle properties and fluidization conditions that govern particle mixing in fluidized beds and directly influence conversion rates and process efficiency.

The bubble flow has shown to play a pivotal role in the solids mixing in fluidized beds [25–29]. Rising bubbles drag both bulk and lean solid particles in their wake, creating regions of upward solids flow. Upon eruption at the dense bed surface, the lifted particles are splashed back onto the bed surface [30,31]. Meanwhile, solids in the suspension around the rising bubbles move downwards to fill the void, creating regions of downward solids flow [32]. The bubbles driving these solids mixing can originate from the excess fluidization gas – called the *exogenous bubbles*. Alternatively, bubbles may evolve from gases released by particles themselves during physical and/or chemical processes (e.g., drying, devolatilization) – in which case they are called *endogenous bubbles*. In the industrial conversion processes described above, these two bubble sources act simultaneously: the fuel particles generate endogenous bubbles as they release gas, while being driven through the bed by the solids circulation induced by the exogenous bubbles.

Previous experimental studies on endogenous bubbles, reviewed in Section 2, have advanced understanding of single-particle lift but share methodological limitations that restrict their applicability to industrial conditions. Most of these investigations focused on buoyant gas-releasing particles fed beneath the surface of a bed at minimum fluidization conditions, thereby making it possible to observe both the formation of distinct endogenous bubbles and unequivocally correlate them to the lifting effect on the studied particles [33–37]. The studies conducted at fluidization velocities beyond minimum fluidization [35] covered a very low fluidization range ($1 \leq u_0/u_{mf} \leq 2$) and faced the challenge of differentiating between endogenous and exogenous bubbles as bubbles of these two types exchange gas and are likely to coalesce. Furthermore, the mixing of solids in the lateral directions, despite its importance in reactor design, remains largely unexplored. In fluidized beds containing several types of solids (e.g., bulk solids and fuel particles), the rate of lateral mixing can vary significantly between solids [38–40], suggesting that gas release may also affect the lateral dispersion of solids.

Fluidized beds aimed at processing gas-releasing solid feedstock (e.g., materials with high moisture and/or volatile content such as biomass, waste, and plastics) typically involve fluidization velocities well above minimum fluidization. These conditions have not been studied in literature. Industrial setups also often use over-bed feeding rather than in-bed feeding considered in previous work. Typical feedstock particles are generally lighter and larger than the bulk solids and tend to segregate to the dense bed due to buoyancy [9,41–45]. Moreover, all the previous studies on gas-releasing particles used spherical particles with gas release across the entire particle surface, whereas gas release from drying and devolatilization of larger biomass particles occurs preferentially along the fiber structure [46]. It results in directional gas release that can have the potential to push the particle by means of a small thrust [47].

The primary aim of this study is to investigate the effect of gas-release on the mixing behavior of particles larger and lighter than bulk solids in a fluidized bed under bubbling conditions. Both axial and lateral mixing are examined along with the net force acting on the particle to quantify the impact of gas release. To achieve this, 3D magnetic particle tracking is employed, enabling non-invasive, high-resolution measurement of particle trajectories. The effect of fluidization velocity, the gas-release rate, and the density and size of the gas-releasing particle are studied under operating conditions relevant to industrial applications (a 0.71 × 0.71 m^2 bed at u_0/u_{mf} = 1.5–5, reproduced through fluid-dynamic scaling).

2. Research Background

The concept of endogenous bubbles was first introduced by Yates *et al.* [48] who, based on empirical observation, suggested that volatiles released from coal particles ascend through the bed in the form of bubbles and proposed modeling their contribution to bed dynamics using the two-phase theory of fluidization. Subsequently, research employing advanced measurement techniques also indicated structural and behavioral similarities between exogenous and endogenous bubbles [49]. Using X-ray imaging at 730 °C under minimum fluidization conditions (thus in the absence of exogenous bubbles), Iannello *et al.* [49] observed that endogenous bubbles formed during the conversion of 12 mm beech wood injected at the bottom of the bed closely resembled the features of exogenous bubbles. These bubbles exhibited a gas-rich core, a surrounding cloud of entrained bulk solids, and a dense wake region beneath them where solids are dragged upward.

Fiorentino *et al.* [33] examined, also under minimum fluidization and in-bed feeding conditions at 850 °C, the impact of endogenous bubbles on the mixing of various fuel particles. They found that gas-releasing particles segregate to the bed surface on timescales much shorter than their devolatilization time. Buoyant particles ascended almost instantaneously, lifted by a single endogenous bubble, whereas heavier particles required multiple endogenous bubbles and therefore rose in a stepwise manner. Ascent times ranged from 2 to 10 s depending on the density and volatile content of the particle and were essentially independent of the particle size of the bulk solids. In contrast, similarly heavy particles did not rise to the bed surface in the absence of gas release or required much longer than 10 s to do so, even in the presence of exogenous bubbles. These findings led to the conclusion that, under minimum fluidization conditions, endogenous bubbles contribute to particle lift and promote faster axial segregation of buoyant particles. Bruni *et. al* [37] extended this work, still under minimum fluidization conditions at 800 °C, using x-ray imaging of biomass particles devolatilizing in a bed of hot sand. They reported that, in the presence of lighter bulk solids with a density comparable to that of the gas-releasing particle, the endogenous bubbles failed to lift the particle, resulting in an oscillatory axial motion instead, and thus did not enhance the segregation. These contrasting results pointed towards a dominant impact of net buoyancy on segregation.

Iannello *et al.* [19] observed that converting plastic particles melted instantly and tended to agglomerate with the bulk solids, remaining near their injection point. This occurred regardless of whether the particles were introduced below or at the bed surface. This behavior contrasts with the biomass or coal particles, which consistently segregate towards the bed surface in the presence of gas-release.

Solimene *et al.* [35] investigated the effect of endogenous bubbles on the upward motion of non-buoyant gas-releasing particles injected at the bottom of the bed at fluidization velocities slightly above minimum ($1 \leq u_0/u_{mf} \leq 2$) in a cold bed. They observed the formation of endogenous bubbles at minimum fluidization conditions and further quantified their contribution to the particle lift at velocities above minimum by estimating the net upward force generated during the bubble growth, which they then termed *lift force*. They also proposed a correlation linking this lift force to the particle size and the gas-release rate, which has since been widely adopted [34,36,50,51]. Iannello *et al.* [36,49] experimentally measured the size of endogenous bubbles (under conditions similar to [27]) and refined the original lift force correlation by introducing a fitting parameter representing the fraction of released gas that contributes to bubble formation.

The momentum flux of gas-releasing particles reflects the intensity of local disturbances imparted to the surrounding bed. Based on the data reported by Solimene *et al.* [35], the calculated momentum flux is relatively high (10^{-5} kg.m/s^2), indicating that the particles strongly influence the local bed hydrodynamics, potentially creating bubbles or jets. Based on the data from Iannello *et al.* [49], the estimated momentum flux is much lower (10^{-6}–10^{-7} kg.m/s^2), suggesting a

comparatively minor contribution to the surroundings of the particle.

3. Methodology

3.1. Experimental setup and procedure

The cold flow model used in this work is designed and operated according to Glicksman's full set of fluid-dynamic scaling laws [52]. The model resembles the gas-solids flow for biomass pyrolysis at 700 °C in a bed of silica sand (760 μm, 2600 kg/m^3) fluidized by flue gas in a unit of 0.71 × 0.71 m^2 and with a static bed height of 0.16 m. Table 1 lists the scaling ratios as well as the operational conditions and the gas and solids properties for both the reference unit and the cold model. With a length scaling factor of 0.26, the cold model has a cross-section of 0.17 × 0.17 m^2 and a bed height of 0.04 m (at rest), consisting of bronze particles (189 μm, 8492 kg/m^3) fluidized by ambient air. The minimum fluidization velocity of the gas-solids pair used in the cold model is 0.084 m/s. Fig. 1 schematizes the cold flow model and the corresponding instruments used in this work. While many fluidized-bed units for endothermic reactions employ cylindrical geometries, square and rectangular cross-sections are common in large-scale fluidized bed systems involving large solids streams, e.g., indirect gasification/pyrolysis or direct reduction of iron ore, where it is cost-advantageous in terms of construction and integration with solids inlets/outlets and for control of the residence time distribution. A representative example is the Chalmers 2–4 MW$_{th}$ indirect biomass gasifier [14], which has a rectangular cross-section.

Two types of solids tracers are used in this study: non-releasing (hereafter called *blank*) and *gas-releasing*. The *blank* tracers are used to capture the dynamics of a large particle immersed in the bed and serve as a control against which the behavior of the *gas-releasing* tracer is evaluated. Rather than focusing on the formation and dynamics of endogenous bubbles, the present work centers on the resulting movement of the particle in response to the gas release. To this end, particle motion is tracked using the non-invasive 3D magnetic particle tracking (MPT) technique [53], implemented with a measurement system provided by the Research Institutes of Sweden (RISE). The MPT system consists of eight sensors mounted on the outer surface of the bed walls, enabling spatial localization of a magnet embedded in the core of the tracer particle (Fig. 1c). Particle positions were resolved with an accuracy of 1 mm at a sampling rate of 100 Hz.

The tracers used have a cylindrical shape with a length-to-diameter ratio of ~1.5. Three tracer classes were used (each of which was engineered in both *blank* and *gas-releasing* versions): (i) *Reference* (size and density representing a typical large biomass pellet or wood chip), (ii) *Larger* (increased size compared to *reference*, representative of coarser woody feedstock such as directly fed wood chunks), and (iii) *Heavier* (increased density compared to *reference*, representative of denser feedstock such as anthracite or densified char/coal). The physical properties of these fuels represented by these tracer classes are plotted in Fig. 2 and contrasted against the properties of typical bed material (Silica Sand or Olivine) and industrial fuel and feedstock particles.

The tracer particles consist of a cylindrical case holding a 3 × 3 mm cylindrical magnet in its center. The *gas-releasing* tracers additionally contain dry ice, which sublimates as CO_2 gas (hereafter referred to as *tracer gas*) and is released from the particle through porous caps at both flat ends of the cylindrical particle, thus mimicking the directional release of moisture and volatiles during biomass drying and devolatilization (Fig. 1b). *Gas-releasing* tracers have the exact same size as their corresponding *blank* counterparts, while density differs by 5–10%, i.e., small enough to assume no significant impact on their mixing behavior. The difference in mass progressively decreases during the experiment as the dry ice sublimates, leading to increasingly similar particle densities. The properties of all 6 different tracer particles are listed in Table 2.

Given the presence of dry ice in the tracers, the bed temperature could potentially drop. However, a thermocouple immersed in the bed registered a stable temperature throughout the experiment and between repetitions. The CO_2 concentration is measured at the outlet duct of the setup using a gas probe. The sampled gas is analyzed in an X-STREAM Gas Analyzer (XEGK, Emerson), and the concentration is logged at 1 Hz. To ensure representative sampling, the gas leaving the unit is homogenized upstream of the sampling position by letting it pass through a section of packings.

The time evolution of the gas flow released by each tracer is presented in Fig. 3, expressed as both superficial velocities at the flat surfaces of the cylindrical particles and as volumetric flowrates. This instantaneous gas-release rate is calculated from a mass balance closure using the total air flow rate injected for fluidization and the CO_2 concentration measured at the outlet duct. The corresponding volumetric flowrates and superficial velocities are derived assuming the gas holds the bed temperature measured by the thermocouple. Uncertainties in the estimated release rates may arise from the imperfect mixing of CO_2 in the outlet gas, potential bypassing of CO_2 through the tracer insertion port, and the asymmetry in the gas release rate from both tracer ends. The characteristic time delay of the gas measurement system is measured beforehand and considered to build the time evolution curves in Fig. 3. The CO_2 concentration in ambient air is deducted as background.

As shown in Fig. 3, the release of CO_2 is not constant throughout the experiment; an initial peak followed by a gradual decrease was consistently observed for all experiments. Based on literature data for smaller biomass particles (5–20 mm), which exhibit devolatilization times of 33–201 s under inert conditions at 560–740 °C [54], expected gas-release velocities can be estimated for biomass particle considered here. For the reference biomass particles resembled here (70 mm, see Table 2), devolatilization times are expected to be 100–200 s for 80% volatile content, yielding expected time-averaged velocities of ~0.06–0.12 m/s. The peak velocities observed here (~ 0.05 m/s) fall slightly below the expected time-averaged release rate but are still considered representative for a considerable part of the devolatilization process. These velocity values are also comparable to the velocity range calculated from the data reported by Iannello *et al.* [49] for 12 mm biomass at 730 °C (0.01–0.1 m/s. For the higher release rates (30 × 10^{-6} m^3/s) of the *reference* tracer, the corresponding momentum flux is on the order of 10^{-5} kg.m/s^2, within the range estimated from previous works [35,49], and so, expected to noticeably affect the local bed hydrodynamics.

Experiments were performed at four fluidization numbers (u_0/u_{mf} =

Table 1
Characteristics of the reference reactor and the corresponding cold model. Fluid-dynamical scaling done according to Glicksman's full set [52].

Parameter		Hot reactor simulated	Cold flow model used
Operational conditions	Temperature [°C]	700	20
	Pressure [atm]	1	1
	Minimum fluidization velocity [m/s]	0.16	0.084
Fluidization gas		Flue gas	Air
	Density [kg/m^3]	0.36	1.20
	Viscosity [N/(m•s)]	4.07 × 10^{-5}	1.83 × 10^{-5}
Bed material bulk solids		Silica sand	Bronze
	Particle density [kg/m^3]	2600	8492
	Mean particle size [mm]	0.789	0.189
Feedstock particle		Wood chips	Tracer
	Particle density [kg/m^3]	300–700	990–2300
	Mean particle size [mm]	1–130	0.26–34
Scaling ratios $\left[\frac{\text{cold}}{\text{hot}}\right]$	Length	0.26	
	Time	0.509	
	Mass	0.06	

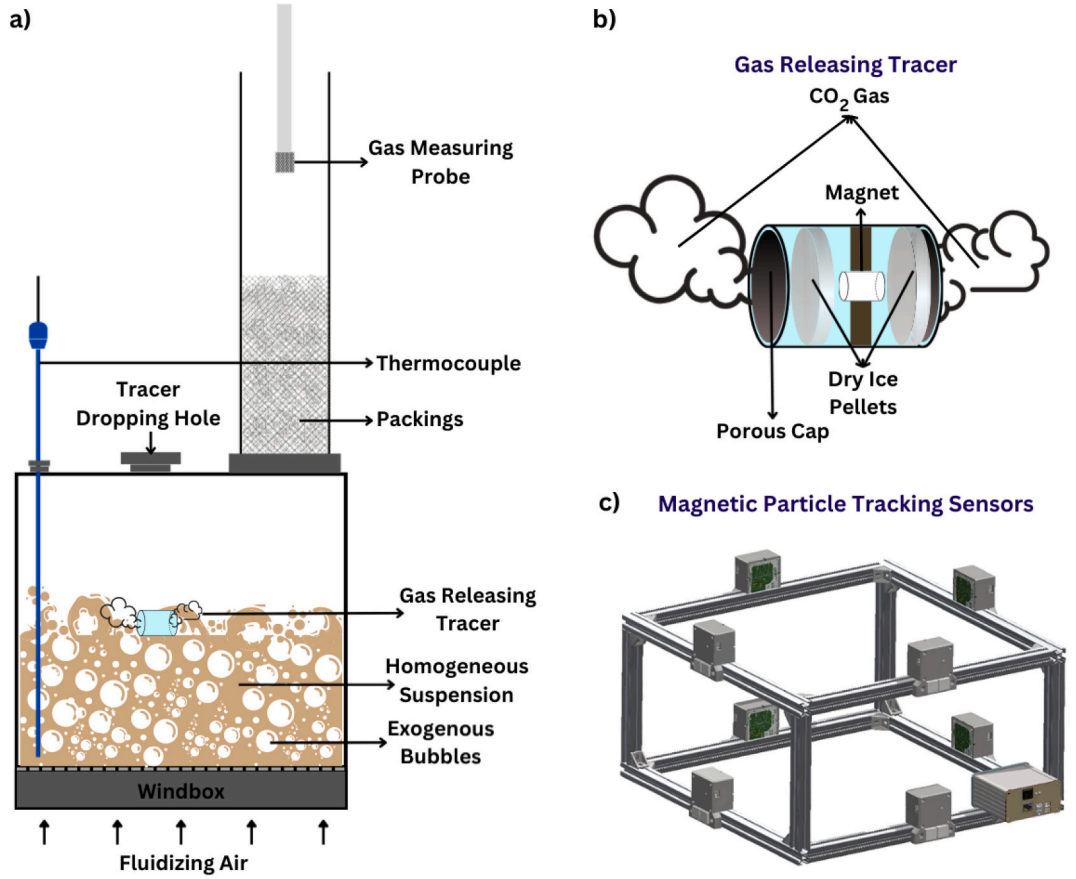

Fig. 1. (a) Schematic of the experimental setup (0.17 × 0.17 m^2 in cross-section) indicating the location of the thermocouple and the gas measurement probe, (b) depiction of the gas-releasing tracer particle, and (c) sensor arrangement for the Magnetic Particle Tracking (MPT) system.

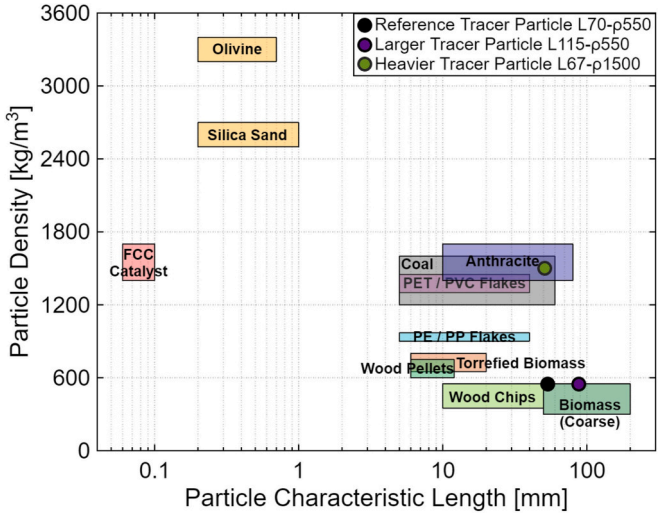

Fig. 2. Property-space map including the three tracer classes used in this work (*Reference* L70 – ρ550, *Larger* L115 – ρ550, *Heavier* L67 – ρ1500) relative to representative industrial fuel/feedstock particles and bed materials.

Table 2
Characteristics of the tracer particles used. All tracers have a length-to-diameter ratio of 1.5.

Tracer Particle Type	Size (cylinder length) [mm]			Density [kg/m^3]	
	Resembled hot condition	Cold down-scaled test		Resembled hot condition	Cold down-scaled test
Reference Tracer Particle L70 – ρ550	70	17	Blank	498	1800
			Gas-releasing	553	2000
Larger Tracer Particle L115 – ρ550	115	28	Blank	525	1900
			Gas-releasing	553	2000
Heavier Tracer Particle L67 – ρ1500	67	16	Blank	1438	5200
			Gas-releasing	1507	5450

1.5–5). The tracer was manually released at 0.12 m above the bed surface (from the tracer dropping hole illustrated in Fig. 1). Preliminary test confirmed that this height has no effect on the resulting movement of the tracer once in the bed. The trajectory acquisition was initiated 6 ± 3 s after the tracer release. The analysis, therefore, focuses on the lateral mixing of lean-phase solids within the bed and excludes the initial bed immersion period. *Blank* tracers are tracked continuously for 60 min, whereas *gas-releasing* tracers are tracked until complete sublimation of dry ice, typically 10–15 min. Each experimental condition is repeated 5 times to ensure the statistical robustness of the data acquired.

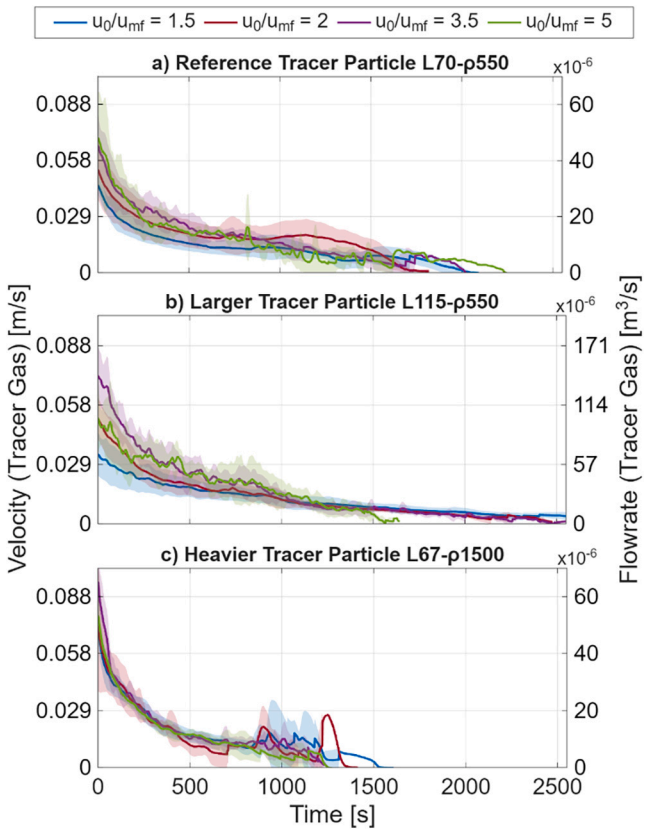

Fig. 3. Time evolution of gas release velocities and corresponding gas release rates for the different tracer types and fluidization velocities. Values in the plot are upscaled using scaling factors listed in Table 1. Shaded regions indicate variability between repetitions. (a) *Reference* tracer L70-ρ550; (b) *Larger* tracer L115-ρ550; and (c) *Heavier* tracer L67-ρ1500.

3.2. Data processing

The tracer trajectory throughout the experiment is provided by the MPT system. The tracer axial positions recorded within the dense bed (i.e., excluding the splash zone) are used to calculate the mixing index, *M*, ranging from 0 (complete segregation) to 1 (perfect mixing), according to:

$$M = 1 - \frac{\sigma_{distribution}}{\sigma_{max}} \quad (1)$$

where, $\sigma_{distribution}$ is the variance of the measured axial distribution of tracer particle positions, and σ_{max} represents the variance at complete segregation (the hypothetical state in which the particle remains confined to a single horizontal layer of the dense bed).

The lateral dispersion coefficient of the lean solids $(D_{x,y})$ is calculated using the Einstein relation for Brownian motion [55]:

$$D_{x,y} = \frac{\Delta_{x,y}^{\ 2}}{2\Delta t} \quad (2)$$

where $\Delta_{x,y}$ is the lateral net displacement over the time interval Δt. To ensure that the calculated dispersion reflects macroscopic mixing, a threshold value of $\Delta_{x,y} = 0.125$ m (upscaled) is used to disregard small-scale motions, following the methodology of [56]. Each time the tracer displacement from the last recorded position exceeds this threshold length, a new dispersion coefficient value is calculated, and the reference position is reset, yielding multiple independent values per trajectory. Further, only conditions where the tracer made at least one qualifying displacement every 10 s on average were included. By differentiating the tracer position in time, the tracer acceleration and, consequently, the net external force acting on it at any given time can be calculated.

4. Results

The acquired trajectories are studied for axial and lateral movement separately, both in aggregated (combining repetitions) and disaggregated (specific trajectories) form. The results presented in this section are shown on an upscaled basis, i.e., applicable to the hot and large-scale conditions listed in Table 1. The three tracer classes — L70-ρ550 and L115-ρ550 representing buoyant biomass feedstocks (wood pellets and barks / branches / residues, respectively) and L67-ρ1500 representing densified char — span the property range of industrial fluidized-bed fuel particles mapped in Fig. 2.

4.1. Axial mixing

Fig. 4 compares the distributions of axial positions of *gas-releasing* and *blank* tracers for all three tracer classes and across four tested fluidization velocities. Irrespective of whether the tracer releases gas or not, the *reference* (L70-ρ550) and *larger* (L115-ρ550) tracers predominantly remained near the bed surface (buoyant behavior), whereas the *heavier* (L67-ρ1500) tracer exhibited substantial immersion within the bed (non-buoyant behavior). Increasing fluidization velocity has a similar effect in all cases: shifting the axial distributions upward, and making it broader (most clearly observable in Fig. 4a). In other words, higher fluidization velocities led to broader axial distributions for all tracers, meaning an enhanced mixing, which is consistent with the trends reported in the literature [10,12].

When comparing *blank* and *gas-releasing* pairs, the effects are different depending on the buoyancy of the particles. For the *reference* (L70-ρ550) and *larger* (L115-ρ550) tracers (Fig. 4a and b), at lower fluidization velocities ($u_0/u_{mf} \leq 2$), the gas-release has the effect of shifting the average vertical location to slightly lower locations (compared to the blank counterparts), indicating the partial immersion of the particles that would otherwise float at the bed surface. This effect weakens with increasing fluidization velocity and becomes negligible at $u_0/u_{mf} \geq 3.5$.

In contrast, gas release strongly affects the distribution of axial positions for the *heavier* (L67-ρ1500) tracer (Fig. 4c). At low fluidization velocities ($u_0/u_{mf} \leq 3.5$), the *blank* tracer is predominantly confined to the lower third of the dense bed, whereas the *gas-releasing* tracer exhibits a significant share of positions near the upper dense bed, particularly at $u_0/u_{mf} = 2$. With increasing fluidization velocity, this difference progressively diminishes until disappearing at $u_0/u_{mf} = 5$, where the axial distributions of *gas-releasing* and *blank* tracers are nearly indistinguishable from each other.

Fig. 5 assesses the effect of the magnitude of the gas release by presenting the mean axial positions of the tracers as a function of the instantaneous gas-release rate. Unlike Fig. 4, which aggregates data of entire experiments (with changing release rates, see Fig. 3), Fig. 5 links the instantaneous axial position and gas-release rate. The case $u_0/u_{mf} = 2$ is taken here as it consistently exhibited the most substantial differences between the *blank* and *gas-releasing* tracers (already perceived in Fig. 4). Higher gas-release rates are represented by relatively fewer data points, as most experimental data correspond to intermediate or lower release rates (see Fig. 3). Data corresponding to the *blank* tracer particles appear at zero gas-release rate (in blue color). The location of the dense bed surface is indicated by the grey-shaded band, for reference.

For the *heavier* (L67-ρ1500) tracer (of rather non-buoyant nature), the magnitude of the gas release shows a clear connection with the axial position. Fig. 5 shows that the *gas-releasing* tracer occupied positions closer to the bed surface compared to the *blank* counterpart, for all, except the higher gas release rates ($> 40 \times 10^{-6}$ m^3/s). Under those conditions, the average position of the *gas-releasing* tracer became similar (or even somewhat lower) than that of the *blank* tracer. The

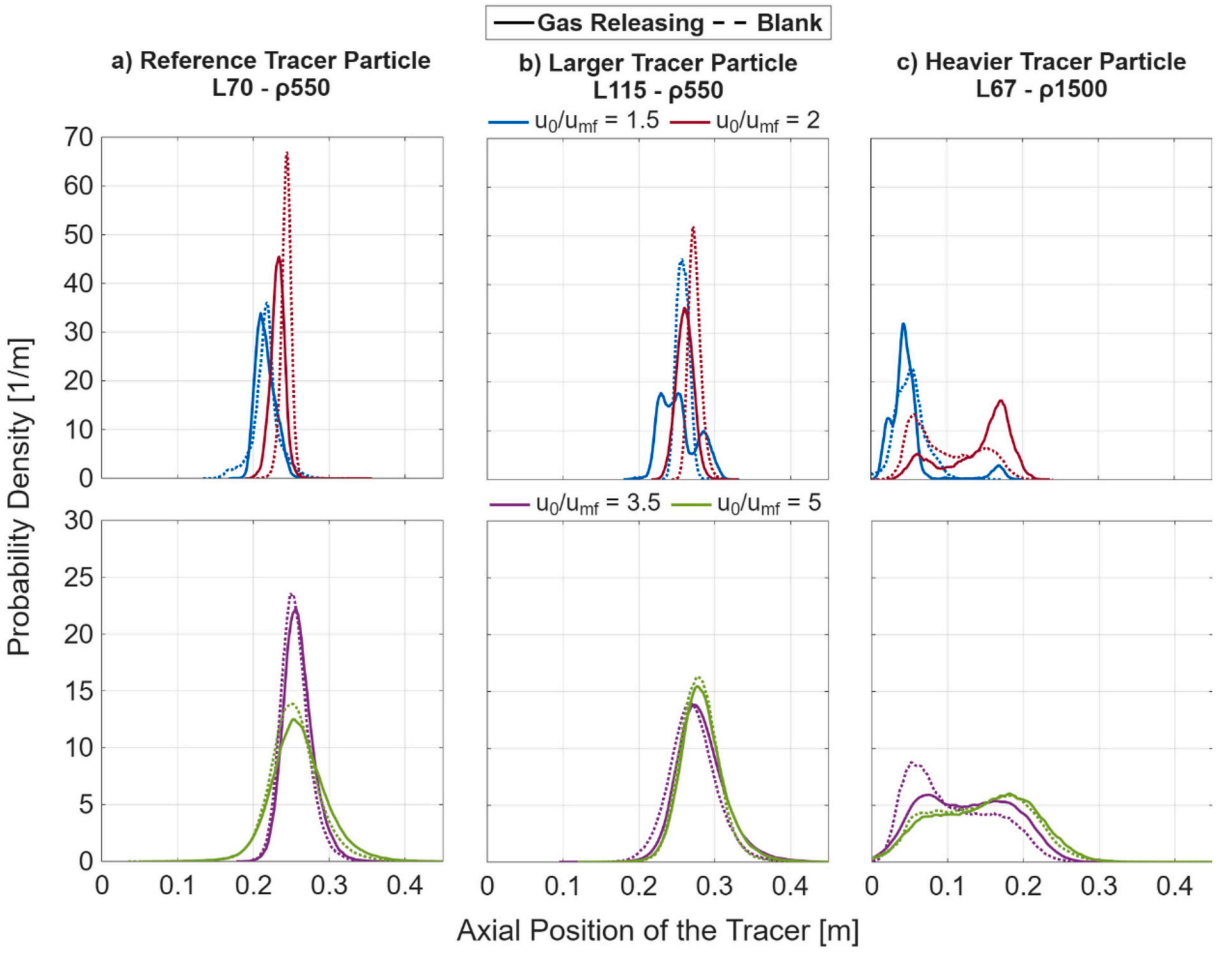

Fig. 4. Probability density function of the axial positions of the tracer particles for different fluidization velocities ($u_0/u_{mf} = 1.5$ and 2 in the upper row, and $u_0/u_{mf} = 3.5$ and 5 in the bottom row); (a) *Reference* (L70-ρ550) tracer; (b) *Larger* (L115-ρ550) tracer; and (c) *Heavier* (L67-ρ1500) tracer.

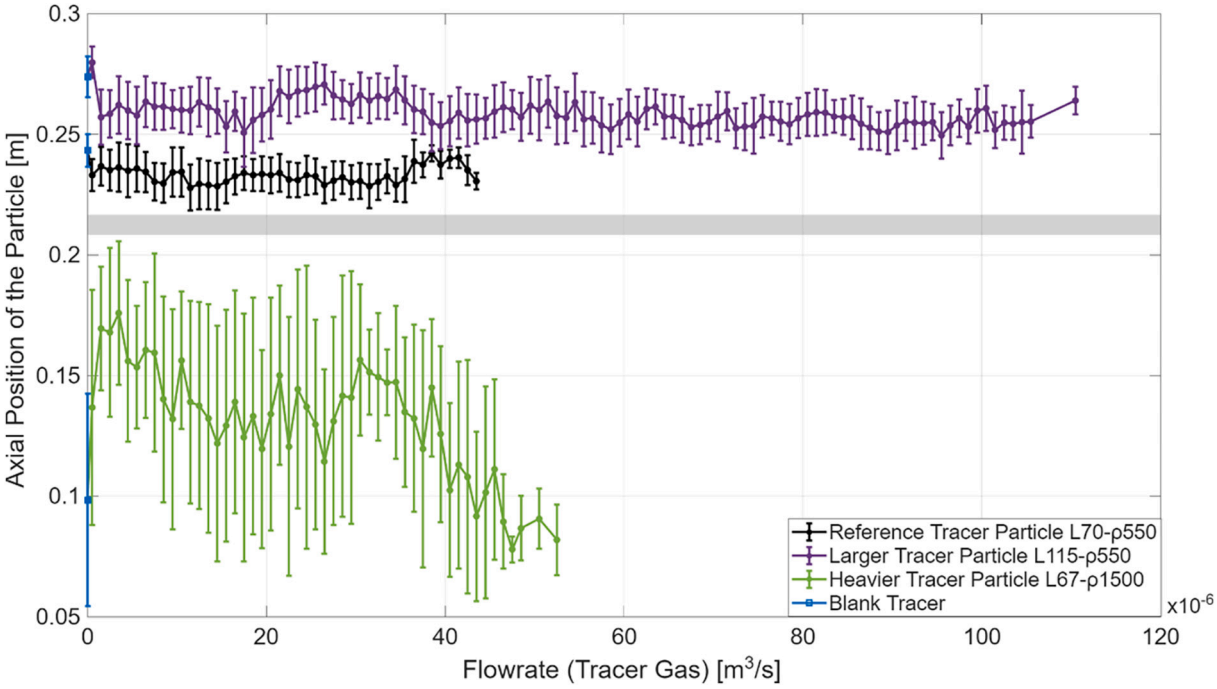

Fig. 5. Axial position of tracers as a function of the release flowrate of tracer gas for $u_0/u_{mf} = 2$. The first bins ($x = 0$ m^3/s) with blue color represent the *blank* tracers. The bars indicate the standard deviation within each release-rate bin. The grey-shaded band indicates the dense-bed height interval at $u_0/u_{mf} = 2$. (For interpretation of the references to color in this figure legend, the reader is referred to the web version of this article.)

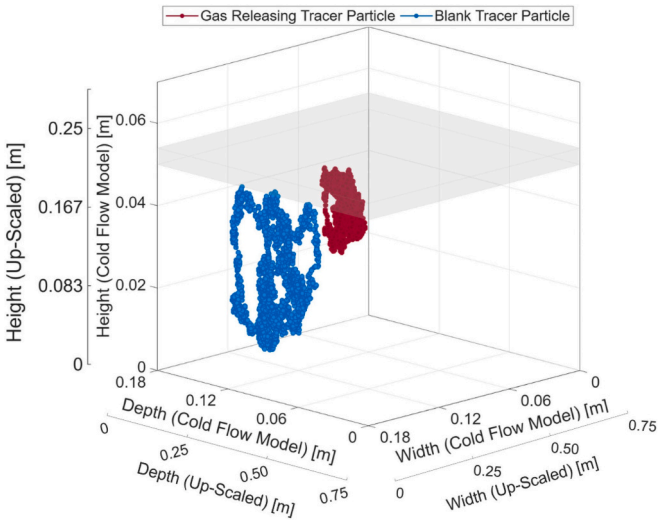

Fig. 6. Selected trajectory sections that exemplify the behavior of *heavier* (L67-ρ1500) tracers for $u_0/u_{mf} = 2$. For the *gas-releasing* tracer, the trajectory corresponds to an intermediate release rate $\approx 30 \times 10^{-6}$ m^3/s. Each trajectory collects 60 s of data. The grey-shaded slice indicates the bed-height interval.

reference (L70-ρ550) tracer (of rather buoyant nature) exhibits the opposite trend and to a lesser extent. At low and intermediate gas-release rates, the *gas-releasing* tracer was located deeper in the bed as compared to the *blank* tracer (though still close to the bed surface), whereas at high gas-release rates their mean axial position becomes similar to that of the *blank* tracer. For the *larger* (L115-ρ550) tracer (also buoyant), the *gas-releasing* tracer consistently exhibited slightly lower average axial positions than its *blank* counterpart across the entire range of gas-release rates.

To shed some light on the actual motion of the particle, the analysis is complemented by examining single trajectories. While the information aggregated from several repetitions identifies the statistically favored regions as a function of the gas release rate, the single trajectory reveals the nature of the underlying displacements. This is done exclusively for the *heavier* (L67-ρ1500) tracer, as it was the one exhibiting the strongest response to gas release. Fig. 6 shows a representative section of the trajectory of the *heavier* (L67-ρ1500) *gas-releasing* tracer at $u_0/u_{mf} = 2$ (as in Fig. 5), at a relatively higher gas-release rate of $\approx 30 \times 10^{-6}$ m^3/s and compares it with the trajectory section of the corresponding blank tracer.

The individual trajectory section shows that the *gas-releasing* tracer has a rather restricted motion, both in axial and lateral directions. While the particle may be found in a range of heights across different

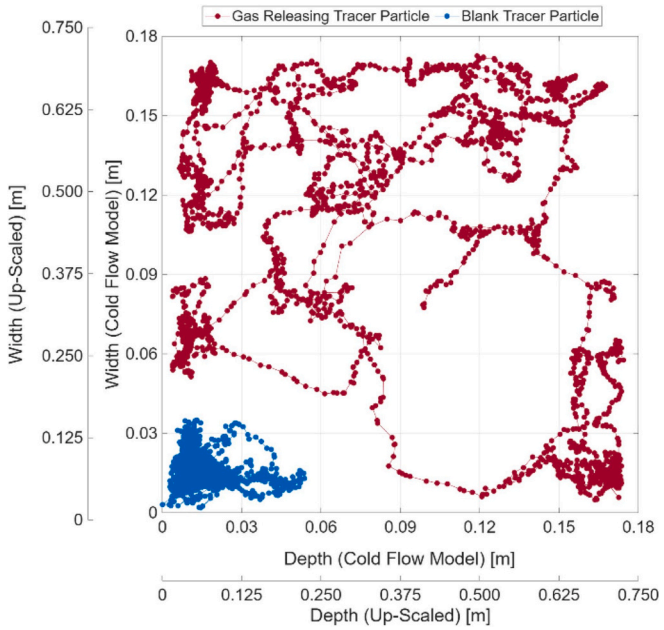

Fig. 8. Top view of the trajectory sections (60 s) of the *reference* (L70-ρ550) tracer for $u_0/u_{mf} = 5$, for both *blank* and *gas-releasing* versions.

experiments, as indicated in Fig. 5, its displacements within a single trajectory remain rather small. In contrast, the *blank* tracer traverses nearly the entire bed height and a large fraction of the lateral cross-section throughout the experiment. Similar restricted motion has been reported by Bruni *et al.* [37] for particles with densities comparable to that of the suspension.

To characterize the general ability of the tracer to mix in the bed and compare different fluidization and gas release conditions, the mixing index is calculated. Fig. 7 shows the mixing index for the *heavier* (L67-ρ1500) tracer at different fluidization velocities and gas-release rates, with the first column representing the *blank* tracer variants. Note that the third row corresponds to the data series plotted in green in Fig. 5. The mixing index increased with fluidization velocity for both *blank* and *gas-releasing* tracers, highlighting the significant impact of the fluidization conditions. At low fluidization velocities ($u_0/u_{mf} \leq 2$), the impact of the gas release becomes more dominant, with increased gas-release rates consistently yielding lower mixing index values than the *blank* counterparts.

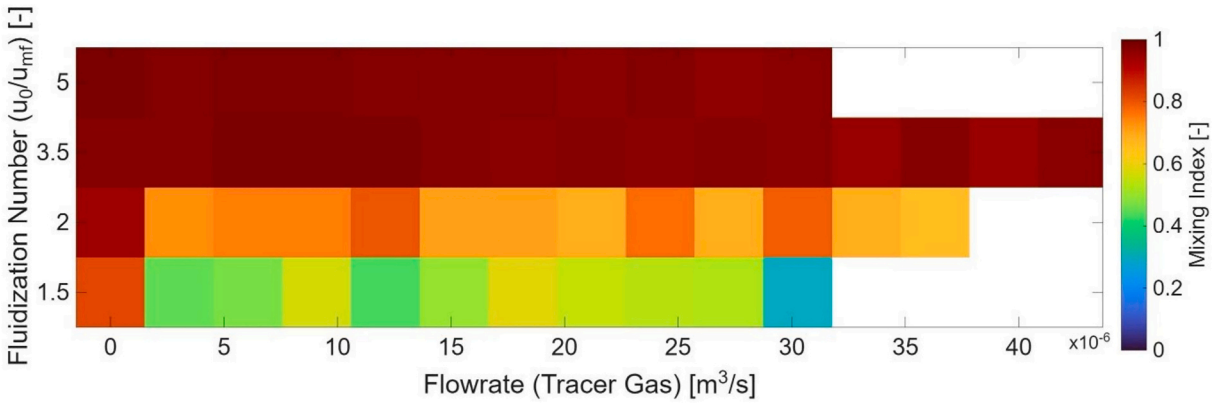

Fig. 7. Mixing index of *heavier* (L67-ρ1500) tracer as a function of the release rate of tracer gas. The first bin (x = 0 m^3/s) represents *blank* tracer particles.

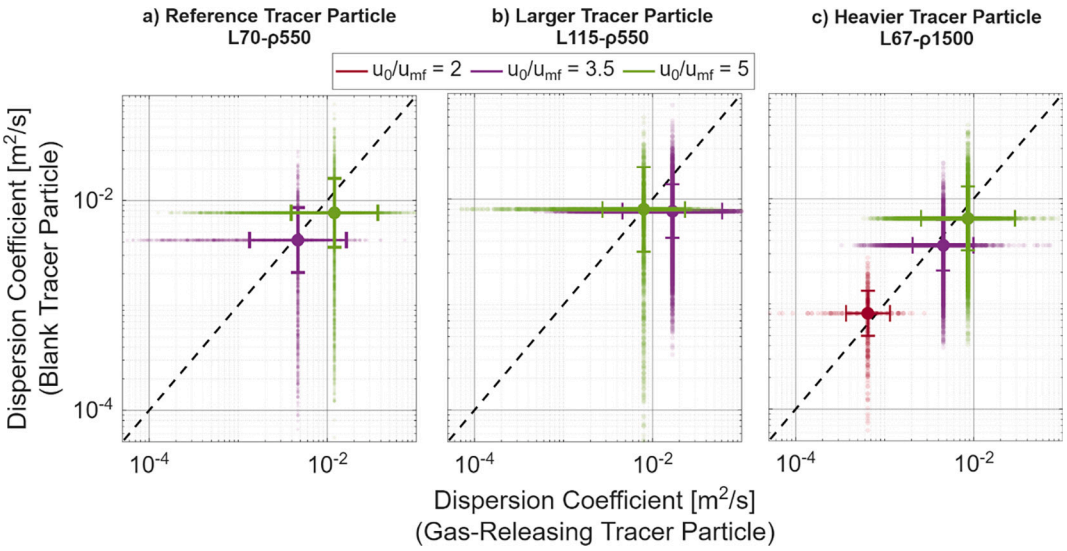

Fig. 9. Lateral particle dispersion coefficients of *blank* and *gas-releasing* tracers, for different fluidization velocities. Markers indicate values yielded by individual displacement-events, and the error bars show the standard deviation of these values for each fluidization condition. The dashed line marks parity (gas = blank).

4.2. Lateral mixing

Gas release affects both the vertical and lateral motion of the particle. Fig. 8 exemplifies lateral trajectories of the *reference* (L70-ρ550) tracer at $u_0/u_{mf} = 5$, comparing its *blank* (blue) and *gas-releasing* (red) variants. As seen, the *blank* tracer tends to remain confined to a relatively small part of the cross-section, with motion predominantly near the corner and along the sidewalls, whereas the *gas-releasing* tracer traverses an extensive part of the bed cross-section.

To quantify the ability of a particle to move and mix laterally, the lateral dispersion coefficient is calculated. Fig. 9 presents this coefficient for the four fluidization velocities tested, comparing values of the *gas-releasing* tracers with their *blank* counterparts. Data for tracers at lower fluidization velocities ($u_0/u_{mf} \leq 2$) are omitted because these particles were stagnant in the bed, invalidating the calculation of a dispersion coefficient that assumes free particle movement. For both *blank* and *gas-releasing* tracers, the lateral dispersion coefficient generally increases with fluidization velocity, consistent with previous studies [39]. In general, *blank* and *gas-releasing* tracers show coefficients of the same order of magnitude; however, gas release typically enhances lateral dispersion by 30–40%, with only a few exceptions: the *larger* (L115-ρ550) tracer at $u_0/u_{mf} = 5$ and the *heavier* (L67-ρ1500) tracer at $u_0/u_{mf} = 2$. Dispersion coefficients resolved by release rate intervals of tracer gas are reported in the appended Fig. A.3.

Understanding that the observed behaviors result from the interactions between the particle and the surroundings, and how this interaction is affected by the gas release, the net forces on the particle are calculated and analyzed statistically. Fig. 10 shows the standard deviations of the net external force acting on the *heavier* (L67-ρ1500) tracer, along each spatial direction, comparing *blank* and *gas-releasing* particles across three representative gas-release rate intervals (high – 30×10^{-6} m^3/s, medium – 20×10^{-6} m^3/s, and low – 10×10^{-6} m^3/s). The other two tracers exhibited similar trends, though with slightly different magnitudes, and are not shown to avoid redundancy. The magnitude of the standard deviations of the net force increases with fluidization velocity for all cases. Differences between *gas-releasing* and *blank* tracers are small across the three gas-release rates, indicating comparable ranges of instantaneous net force fluctuations.

5. Discussion

In the following discussion, the tracer classes are referred to as "*lighter*" and "*heavier*" (relative to the bulk solids) to keep the argument applicable to fuel-mixing in general. The three tracers correspond to specific industrial fuel particles: the *Reference* (L70-ρ550) represents wood pellets, the *Larger* (L115-ρ550) represents bark, branches, and other coarse residues, and the *Heavier* (L67-ρ1500) represents densified char.

The motion of a particle immersed in a fluidized bed results from its continuous momentum exchange with the surrounding gas-solids suspension. Consequently, the properties of both the particle and the bed, along with the prevailing bed dynamics, play a major role. Within this momentum balance, one can make a division between surface forces (like the drag force, determined by the relative velocity and solids concentration of the immediate surrounding) and body (volume) forces (like the net buoyancy of the particle relative to the bed, determined by the density difference between the particle and the solids concentration in its immediate surrounding), where the relative significancy of the latter increases with the size of the particle studied (as the volume-to-surface ration increases).

In the absence of gas release, the motion of large particles is governed by the competition between buoyancy and drag. At low fluidization velocities ($u_0/u_{mf} \leq 2$), buoyancy dominates: *blank* lighter (buoyant) tracers remain near the bed surface, while heavier (non-buoyant) tracers immerse into the dense bed (Fig. 4a–c). This behavior is consistent with previous studies [11,12,57–60] and reflects conditions under which volume forces exert a stronger influence on particle motion. Increasing the fluidization velocity ($u_0/u_{mf} \geq 3.5$) strengthens the convective motion (velocities) in the bulk solids resulting in increased drag forces, promoting both axial and lateral transport [28,51]. Consequently, tracer axial distributions broaden (Fig. 4) and lateral dispersion increases (Fig. 9).

When the particle releases gas, the outward gas flux (Stefan flow) is expected to modify the local momentum exchange between the particle and the surrounding suspension [13,33,35–37]. The underlying hypothesis is that the released gas would displace nearby solids and could create small, transient gas pockets near the release points at the longitudinal ends of the particle [46]. As a result, the solids volume fraction in these regions would decrease, producing local variations in the forces that act on the particle, in particular, the effective downward drag force acting on the particle would be weakened [61]. If the gas flow is sufficiently high, it could induce an upward motion of the surrounding bulk solids within the released-gas flow field. This upward bulk solids motion could lift the *gas-releasing* particle upwards towards the bed surface, a

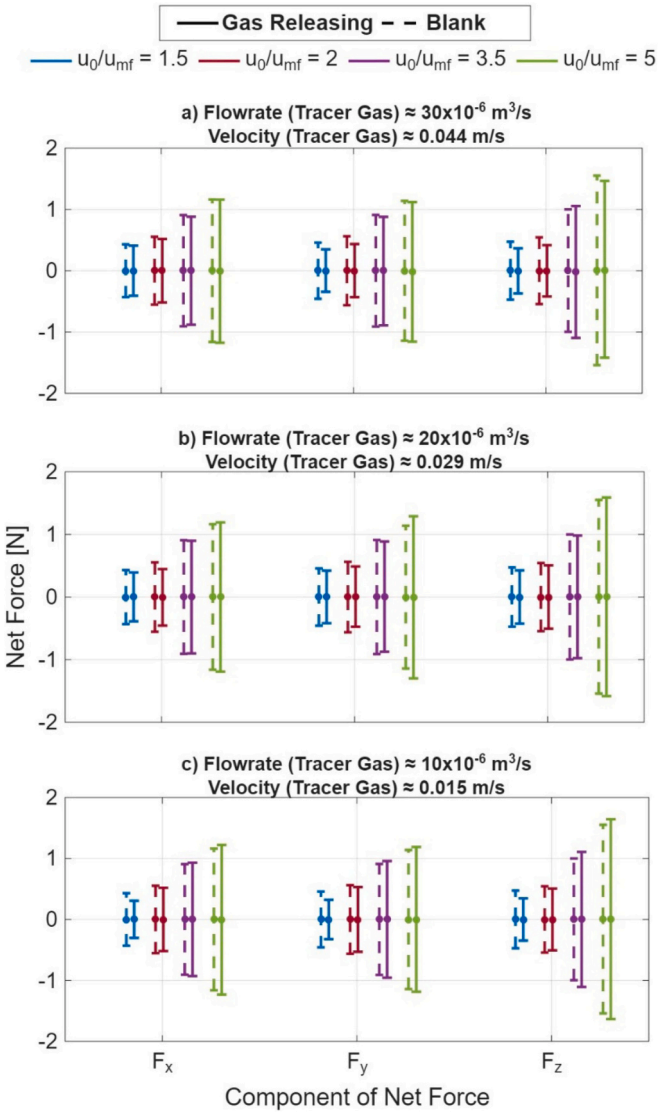

Fig. 10. Comparison of net force components acting on the *heavier* (L67-ρ1500) tracer as a function of fluidization velocity. Bars correspond to the standard deviation. Flowrate of tracer gas released: a) high — 30 × 10^{-6} m^3/s; b) medium — 20 × 10^{-6} m^3/s; and c) low — 10 × 10^{-6} m^3/s.

mechanism often described in the literature as pseudo buoyancy or a lift force [35,37,62]. These modified hydrodynamic interactions would lead to a shift in the preferred axial position of the particle relative to the non-releasing counterparts (Fig. 4), as discussed below.

Fluidization velocity is shown to modulate the extent of the impact of gas release as seen in Fig. 4. The gas release can significantly impact on the vertical distribution of the particle at low fluidization velocities (top-row plots), while the impact is hardly noticeable at higher fluidization velocities (bottom-row plots).

At low fluidization velocities, $u_0/u_{mf} \leq$ 2–3.5, where bulk solids convection is weaker and the bed remains relatively dense, the gas voids originating from the gas release may persist long enough to produce a noticeable local increase in voidage around the particle. Under these conditions of relatively low downward drag, the impact of the gas release on the particle's behavior depends primarily on the particle's body forces (i.e. net buoyancy). For *lighter* (buoyant) particles floating near the bed surface, gas release displaces surrounding solids and causes a slight downward shift in the mean vertical position of the particle (Fig. 4a–b). For *heavier* (non-buoyant) particles fully immersed in the suspension (Fig. 4c) the released gas is expected to rise in the bed as a region of high voidage, thus inducing a local rearrangement of the bulk solids in its wake that effectively pushes the particle up by drift. This mechanism is analogous to the entrainment induced by exogenous bubbles [30] and also reported previously in literature [33,35–37]. This pseudo buoyancy provides the heavier *gas-releasing* particles with an extra lift that shifts its vertical distribution upward in the bed in comparison to the *blank* counterpart (see Figs. 4c and 5). In contrast to the *lighter* particles, this lift is insufficient to bring the *heavier* particle near the bed surface, but the combination of the negative buoyancy and the asymmetric gas release (which might generate alternating void formation) are likely to contribute to the fluctuations in net vertical force experienced by the particle. This yields an alternation of upward and downward motions and thus a sort of vertical circulation. These vertical excursions, however, remain limited in extent compared with the vertical mixing of the *blank* counterpart (Fig. 6), consequently, yielding a lower mixing index as reported in Fig. 7.

At high fluidization velocities, $u_0/u_{mf} \geq$ 2–3.5, bulk solids convection intensifies, and the fluidization gas gains more ability to sweep away the gas released from the particle. Under these conditions, the sustained formation of high-voidage regions around the particle is minimized or prevented altogether. As a result, gas release produces little or no modification of the particle immediate surround, thus yielding no significant impact on the effective drag nor buoyancy. Consistent with the literature [61], the effects of Stefan flow on the mixing of the larger *gas-releasing* particles become negligible beyond a certain fluidization number ($u_0/u_{mf} > 2$ for *lighter* particles and $u_0/u_{mf} > 3.5$ for *heavier* particles, according to Fig. 4). While these threshold values are specific to the particle and bed properties studied here, a similar trend is expected for other systems. Above these thresholds, particle axial motion is governed primarily by the bubble-induced circulation of the bulk solids, with upward transport in bubble wakes balanced by downward motion in the surrounding dense emulsion phase [63]. Prior studies have shown that Stefan-flow effects weaken both at high solids holdup and at high particle Reynolds number [61,64,65], corresponding to conditions where the gas released is either strongly confined by dense solids or rapidly advected away by the surrounding gas flow. Consistent with these findings, the present results indicate that gas-release effects are, across all particle types, noticeable for $u_0/u_{mf} \leq$ 3.5 and most pronounced at $u_0/u_{mf} = 2$.

Regarding mixing in the lateral direction, the impact of gas release manifests at higher fluidization velocities by enhancing the lateral dispersion (Figs. 8 and 9). This is likely associated with the asymmetric gas release [47] between the particle ends, which induces repeated and random small lateral displacements that increase lateral dispersion beyond that experienced by *blank* tracers. This increase in lateral dispersion due to the gas release is substantial under those conditions for which the axial mixing is not significantly impacted, e.g., $u_0/u_{mf} \geq 3.5$, see Fig. 4c and Fig. 9c.

Gas release does not significantly alter the fluctuations in the net force experienced by the particles, as shown in Fig. 10. Instead, the local perturbations in drag and buoyancy induced by gas release manifest as shifts in the preferred axial position and spatial distribution, i.e. the gas release makes the tracer find a new likely location/distribution in the bed where it experiences similar force dynamics. While our measurements reveal the particle trajectories and spatial distributions, they do not sample the instantaneous properties of the gas-solids suspension surrounding the particle, such as voidage or velocity. Consequently, the contributions of modified buoyancy and drag due to gas release cannot be quantified. Future work combining the present trajectory tracking with local measurements or simulations of the particle surrounding is therefore needed to fully characterize how the gas release alters the motion of larger particles in fluidized beds.

6. Conclusion

The influence of particle-generated gas on the mixing of larger

particles in a bubbling bed was investigated under different fluidization velocities and for varying particle size and density, with the particles being fed over the bed surface. Magnetic particle tracking was employed in a fluid-dynamically downscaled unit to extract the motion of such larger particles, investigating both gas-releasing and non-releasing particles. Gas release was attained by dry ice sublimating from cylindrical particle tracers.

Results show that axial particle distribution is primarily governed by particle density relative to the bed, while particle size plays a secondary role. At low fluidization velocities, the buoyant particles (reference tracer) experience a slight downward displacement into the dense bed as gas-induced voids displace solids beneath them, which has been observed during experimental runs. Particles of bigger size than the reference tracer (*larger* tracer) exhibit the same axial behavior, indicating that particle size has a limited effect on axial mixing under low fluidization conditions. Non-buoyant particles of higher density (*heavier* tracer), on the contrary, shift upwards their axial distribution along the bed height upon gas release and exhibit a more restricted axial circulation than their counterparts not releasing any gas.

As fluidization velocity is increased, the intensification of bulk solids mixing fades the influence of gas release on the axial motion of the tracer particles, disappearing beyond certain thresholds ($u_0/u_{mf} > 2$ for buoyant and larger particles, and $u_0/u_{mf} > 3.5$ for heavier particles). Instead, beyond these thresholds, the lateral dispersion of the tracer particles is enhanced through small asymmetric impulses.

The fluctuations of the net force experienced by the tracer particles are dominated by fluidization velocity rather than particle-generated gas release. Thus, under specific conditions, a particle may modify its spatial distribution upon gas release, but the new distribution adopted is such that the dynamics of the net force experienced remain almost unvaried.

CRediT authorship contribution statement

Azka Rizwana Siddiqui: Writing – original draft, Methodology, Investigation, Formal analysis, Data curation, Conceptualization. **Jing Shi:** Writing – review & editing, Investigation, Data curation. **Anna Köhler:** Writing – review & editing, Supervision, Methodology, Conceptualization. **Diana Carolina Guío-Pérez:** Writing – review & editing, Supervision, Methodology, Conceptualization. **David Pallarès:** Writing – review & editing, Supervision, Methodology, Funding acquisition, Conceptualization.

Declaration of competing interest

The authors declare the following financial interests/personal relationships which may be considered as potential competing interests:

David Pallares reports financial support was provided by Swedish Energy Agency. If there are other authors, they declare that they have no known competing financial interests or personal relationships that could have appeared to influence the work reported in this paper.

Acknowledgment

This research was supported by the Swedish Energy Agency through the project “Large-scale production of biocarbon as renewable feedstock in fossil-free value chains within the iron and steel industry” (P2022-00212). The authors also wish to thank research scientist and project manager Fredrik Ahrentorp (Research Institutes of Sweden, RISE) for his contribution in designing the magnetic particle tracking (MPT) system employed in this study.

Appendix A

This appendix complements the data shown in Figs. 4 and 9. Fig. A1 provides the distributional statistics (median, quartiles, and event counts) that characterize the underlying populations.

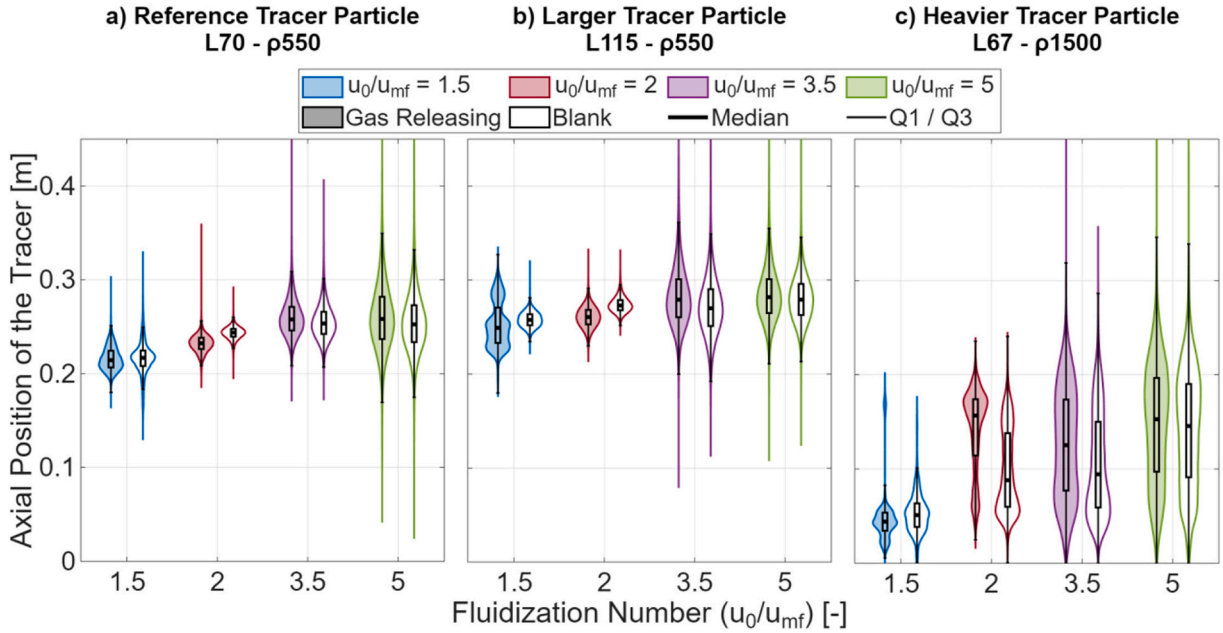

Fig. A.1. Violin plots of the vertical tracer position for the three tracer classes, the *blank* and *gas-releasing* modes, and the four fluidization velocities tested (Complementary to Fig. 4 in the main text). Each violin shows the kernel density estimate of the position distribution; the horizontal bar inside each violin marks the median. Values are reported on an upscaled basis.

Table A.1 provides the numerical distributional statistics of the vertical tracer position for every condition shown in Fig. 4 and Fig. A.1, including

the median, quartiles, IQR, skewness, and sample size. For unimodal distributions, the skewness value quantifies the lopsidedness of the single peak; for bimodal or trimodal distributions (notable at several conditions of the *heavier* tracer), a single skewness value does not faithfully describe the distributional shape and should be interpreted alongside the corresponding violin plot in Fig. A.1.

Table A.1
Distributional statistics of the vertical tracer position [m] for the three tracer classes in the *blank* and *gas-releasing* modes, and all the fluidization velocities tested (Complementary to Fig. 4 in the main text). Values are reported on an upscaled basis.

Particle	FN	Mode	Median	Q1	Q3	IQR	Skewness	Datapoints
Reference Tracer Particle L70 – ρ550	1.5	Gas-Releasing	0.2144	0.2067	0.2244	0.0178	0.498	476,705
		Blank	0.2168	0.2082	0.2247	0.0166	−0.052	399,910
	2	Gas-Releasing	0.2325	0.2263	0.2382	0.0119	−0.067	437,414
		Blank	0.2437	0.2394	0.2477	0.0083	−0.31	359,985
	3.5	Gas-Releasing	0.2578	0.2461	0.2712	0.0251	0.598	420,665
		Blank	0.2535	0.2424	0.266	0.0236	0.617	358,999
	5	Gas-Releasing	0.2583	0.2369	0.2819	0.045	0.331	377,261
		Blank	0.2527	0.2337	0.273	0.0393	0.396	316,591
Larger Tracer Particle L115 – ρ550	1.5	Gas-Releasing	0.2492	0.2332	0.2708	0.0376	0.426	697,422
		Blank	0.2577	0.252	0.2636	0.0116	0.269	361,733
	2	Gas-Releasing	0.2606	0.2529	0.2682	0.0153	0.064	574,660
		Blank	0.273	0.2679	0.2787	0.0108	0.588	362,460
	3.5	Gas-Releasing	0.2791	0.2605	0.3008	0.0404	0.712	699,452
		Blank	0.27	0.2511	0.2903	0.0392	0.396	360,014
	5	Gas-Releasing	0.2819	0.265	0.301	0.036	0.633	390,236
		Blank	0.2791	0.2628	0.2959	0.0331	0.374	360,074
Heavier Tracer Particle L67 – ρ1500	1.5	Gas-Releasing	0.0442	0.0345	0.0538	0.0192	2.594	330,956
		Blank	0.0511	0.0386	0.0636	0.025	0.9	332,886
	2	Gas-Releasing	0.1567	0.1143	0.174	0.0596	−0.8	277,425
		Blank	0.0881	0.0599	0.1381	0.0782	0.398	243,766
	3.5	Gas-Releasing	0.1253	0.0771	0.1737	0.0966	0.121	296,820
		Blank	0.0945	0.0592	0.15	0.0909	0.467	370,210
	5	Gas-Releasing	0.1528	0.0972	0.1966	0.0995	−0.061	316,287
		Blank	0.1456	0.0913	0.1902	0.0989	0.024	363,532

Fig. 9 reports the average value and standard deviation of the distribution of lateral dispersion coefficients calculated for each condition, directly comparing gas-releasing to their *blank* counterparts. In virtue of the fact that some distributions exhibit some degree of skewness, Fig. A.2 reports the median of each case (applied to the same populations of Fig. 9). For most conditions, the two summaries are in close agreement, and the *gas-releasing* versus *blank* counterpart trend is preserved; the only condition where the mean and median differ noticeably is the *Reference* tracer (L70-ρ550) at $u_0/u_{mf} = 3.5$, where the right-skewed tail of the distribution shifts the mean above the median. In spite of this, the conclusions drawn in the discussion remain unaffected.

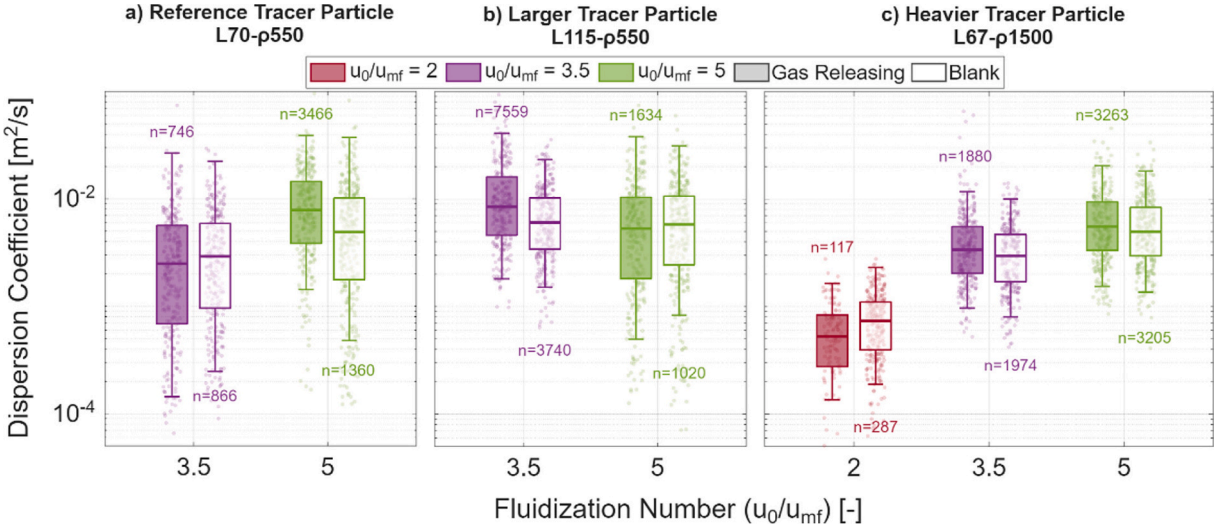

Fig. A.2. Distributions of the lateral dispersion coefficient for the three tracer classes at $u_0/u_{mf} = 2$, 3.5, and 5, shown as boxplots for the *blank* and *gas-releasing* modes (side by side) (Complementary to Fig. 9 in the main text). Each box shows the median, Q1, and Q3; whiskers extend to the minimum and maximum data points within 1.5 × IQR, and points beyond are plotted individually as outliers. The population size (corresponding to the number of qualifying displacement events) per condition is annotated for each box.

The full distributions of lateral dispersion coefficients grouped by CO_2 release rate are presented in Fig. A.3, elaborating on the mean values presented in Fig. 9 and Fig. A.2. No consistent trend is observed between the CO_2 release rates and the dispersion coefficient. The sample counts (n), however, reflect a notable asymmetry: higher release rates ($> 20 \times 10^{-6}$ m^3/s) occur only briefly (consistent with Fig. 3) but generate many qualifying displacement events due to high tracer mobility. In contrast, lower release rates span longer periods yet yield fewer valid values as tracer mobility

diminishes. Thus, it can be said that the higher release rates are the main responsible for the trends observed in Fig. 9 and Fig. A.2. The *blank* tracer, measured over a significantly longer periods than any *gas-releasing* condition, correspondingly shows the largest sample counts at 0 m^3/s."

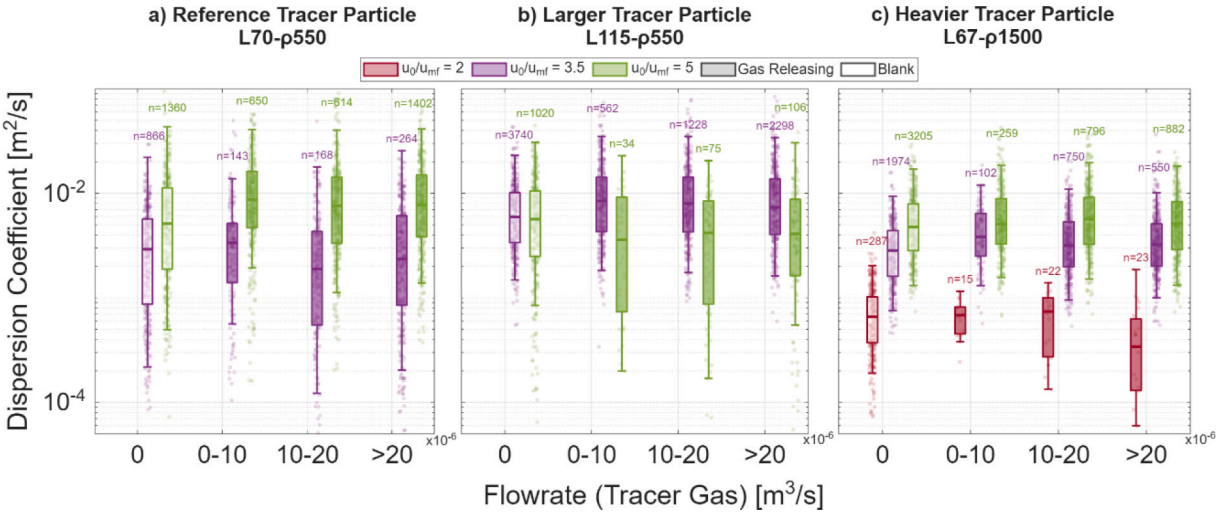

Fig. A.3. Lateral dispersion coefficients as a function of the CO_2 release rate and presented as distributions for the three tracer types at different fluidization velocities (u_0/u_{mf}). The *blank* tracer dispersion coefficient is shown at 0 m^3/s. Boxes represent the interquartile range (IQR), the horizontal line within each box denotes the median, and whiskers extend to the most extreme non-outlier values within 0.75 × IQR from Q1 and Q3. Transparent markers show the distribution of individual dispersion events.

Data availability

Data will be made available on request.

References

[1] D. Kunii, O. Levenspiel, Industrial Applications of Fluidized Beds, in: Fluid. Eng., Elsevier, 1991, pp. 15–59, https://doi.org/10.1016/B978-0-08-050664-7.50008-1.

[2] F. Winter, B. Schratzer, Applications of fluidized bed technology in processes other than combustion and gasification, in: Fluid. Bed Technol. Near-Zero Emiss. Combust. Gasif., Elsevier, 2013, pp. 1005–1033, https://doi.org/10.1533/9780857098801.5.1005.

[3] O. Dogu, M. Pelucchi, R. Van de Vijver, P.H.M. Van Steenberge, D.R. D'hooge, A. Cuoci, M. Mehl, A. Frassoldati, T. Faravelli, K.M. Van Geem, The chemistry of chemical recycling of solid plastic waste via pyrolysis and gasification: state-of-the-art, challenges, and future directions, Prog. Energy Combust. Sci. 84 (2021) 100901, https://doi.org/10.1016/j.pecs.2020.100901.

[4] J.R. Grace, X. Bi, N. Ellis, Essentials of Fluidization Technology, 2020, https://doi.org/10.1002/9783527699483.

[5] J.L.-P. Chen, D.L. Keairns, Particle segregation in a fluidized bed, Can. J. Chem. Eng. 53 (1975) 395–402, https://doi.org/10.1002/cjce.5450530407.

[6] G. Yang, D. Zheng, J. Zhou, Y. Zhao, Q. Chen, Air classification of moist raw coal in a vibrated fluidized bed, Miner. Eng. 15 (2002) 623–625, https://doi.org/10.1016/S0892-6875(02)00057-2.

[7] H. Zhu, P. Lettieri, M. Materazzi, Systematic analysis of mixing and segregation patterns of binary mixtures in fluidised beds for multi-functional processes, Powder Technol. 449 (2025) 120419, https://doi.org/10.1016/j.powtec.2024.120419.

[8] X. Zhu, X. Jiang, Y. Liu, Z. Wang, H. Wang, R. Ocone, Mixing/segregation characteristics and bubble behaviors of density-segregated binary particles in a pressurized fluidized bed, Powder Technol. 434 (2024) 119367, https://doi.org/10.1016/j.powtec.2024.119367.

[9] A. Köhler, A. Rasch, D. Pallarès, F. Johnsson, Experimental characterization of axial fuel mixing in fluidized beds by magnetic particle tracking, Powder Technol. 316 (2017) 492–499, https://doi.org/10.1016/j.powtec.2016.12.093.

[10] F. Fotovat, R. Ansart, M. Hemati, O. Simonin, J. Chaouki, Sand-assisted fluidization of large cylindrical and spherical biomass particles: experiments and simulation, Chem. Eng. Sci. 126 (2015) 543–559, https://doi.org/10.1016/j.ces.2014.12.022.

[11] M. Wirsum, F. Fett, N. Iwanowa, G. LGBRjanow, Particle mixing in bubbling fluidized beds of binary particle systems, Powder Technol. 120 (2001) 63–69, https://doi.org/10.1016/S0032-5910(01)00348-5.

[12] P.N. Rowe, A.W. Nienow, Particle mixing and segregation in gas fluidised beds. A review, Powder Technol. 15 (1976) 141–147, https://doi.org/10.1016/0032-5910(76)80042-3.

[13] P. Salatino, R. Solimene, Mixing and segregation in fluidized bed thermochemical conversion of biomass, Powder Technol. 316 (2017) 29–40, https://doi.org/10.1016/j.powtec.2016.11.058.

[14] H. Thunman, M.C. Seemann, First experiences with the New Chalmers Gasifier BT, in: G. Yue, H. Zhang, C. Zhao, Z. Luo (Eds.), Proceedings of the 20th International Conference on Fluidized Bed Combustion, Springer Berlin Heidelberg, Berlin, Heidelberg, 2010, pp. 659–663.

[15] H. Thunman, M. Seemann, T.B. Vilches, J. Maric, H. Ström, G. Berndes, Advanced biofuel production via gasification – lessons learned from 200 man-years of research activity with Chalmers ' research gasifier and the citation for the original published paper (version of record): advanced biofuel production via gasification – lessons years of research activity with Chalmers ' research gasifier and the GoBiGas demonstration plant 6 (2018) 6–34, https://doi.org/10.1002/ese3.188.

[16] A. Oasmaa, J. Lehto, S. Kallio, Historical Review on VTT Fast Pyrolysis Bio-oil Production and Upgrading, 2021, https://doi.org/10.1021/acs.energyfuels.1c00177.

[17] L. Lundberg, P.A. Tchoffor, D. Pallarès, R. Johansson, H. Thunman, K. Davidsson, In fl uence of surrounding conditions and fuel size on the gasi fi cation rate of biomass char in a fl uidized bed 144 (2016) 323–333, https://doi.org/10.1016/j.fuproc.2016.01.002.

[18] L. Lundberg, A. Soria-verdugo, D. Pallarès, R. Johansson, H. Thunman, The role of fuel mixing on char conversion in a fl uidized bed, Powder Technol. 316 (2017) 677–686, https://doi.org/10.1016/j.powtec.2016.10.060.

[19] S. Iannello, A. Sebastiani, M. Errigo, M. Materazzi, The behaviour of plastic particles during pyrolysis in bubbling fluidized bed reactors: Incipient agglomeration and axial segregation, Powder Technol. 441 (2024) 119846, https://doi.org/10.1016/j.powtec.2024.119846.

[20] S. Iannello, A. Friso, F. Galvanin, M. Materazzi, A Hybrid Physics – Machine Learning Approach for Modeling Plastic – Bed Interactions during Fluidized Bed Pyrolysis, 2025, https://doi.org/10.1021/acs.energyfuels.4c05870.

[21] M.L. Mastellone, U. Arena, Bed Defluidisation during the Fluidised Bed Pyrolysis of Plastic Waste Mixtures * 85, 2004, https://doi.org/10.1016/j.polymdegradstab.2003.04.002.

[22] W. Sun, Y. Yan, Y. Wei, J. Ma, Z. Niu, G. Hu, Catalytic Pyrolysis of Biomass: A Review of Zeolite, Carbonaceous, and Metal Oxide Catalysts, 2025, pp. 1–22.

[23] G. Yildiz, W. Prins, Perspectives of Biomass Catalytic Fast Pyrolysis for Co-refining : Review and Correlation of Literature Data from Continuously Operated Setups, 2023, https://doi.org/10.1021/acs.energyfuels.2c02389.

[24] I. Muhammad, G. Manos, Improving the Conversion of Biomass in Catalytic Pyrolysis via Intensification of Biomass — Catalyst Contact by Co-Pressing, 2021.

[25] I.N.M. Woollard, O.E. Potter, Solids mixing in fluidized beds, AICHE J. 14 (1968) 388–391, https://doi.org/10.1002/aic.690140310.

[26] J. Werther, O. Molerus, The local structure of gas fluidized beds -II. The spatial distribution of bubbles, Int. J. Multiphase Flow 1 (1973) 123–138, https://doi.org/10.1016/0301-9322(73)90008-6.

[27] C.N. Lim, M.A. Gilbertson, A.J.L. Harrison, Bubble distribution and behaviour in bubbling fluidised beds, Chem. Eng. Sci. 62 (2007) 56–69, https://doi.org/10.1016/j.ces.2006.08.034.

[28] N. Mostoufi, J. Chaouki, Local solid mixing in gas-solid fluidized beds, Powder Technol. 114 (2001) 23–31, https://doi.org/10.1016/S0032-5910(00)00258-8.

[29] Z. Amiri, S. Movahedirad, M. Shirvani, Particles mixing induced by bubbles in a gas-solid fluidized bed, AICHE J. 62 (2016) 1430–1438, https://doi.org/10.1002/aic.15150.

[30] P.N. Rowe, B.A. Partridge, An X-ray study of bubbles in fluidised beds, Chem. Eng. Res. Des. 75 (1997) S116–S134, https://doi.org/10.1016/S0263-8762(97)80009-3.

[31] K.S. Lim, P.K. Agarwal, Circulatory motion of a large and lighter sphere in a bubbling fluidized bed of smaller and heavier particles, Chem. Eng. Sci. 49 (1994) 421–424, https://doi.org/10.1016/0009-2509(94)87014-4.
[32] M. Stein, Y.L. Ding, J.P.K. Seville, D.J. Parker, Solids motion in bubbling gas fluidized beds, Chem. Eng. Sci. 55 (2000) 5291–5300, https://doi.org/10.1016/S0009-2509(00)00177-9.
[33] M. Fiorentino, A. Marzocchella, P. Salatino, Segregation of fuel particles and volatile matter during devolatilization in a fluidized bed reactor—II. Experimental, Chem. Eng. Sci. 52 (1997) 1909–1922, https://doi.org/10.1016/S0009-2509(97)00019-5.
[34] S. Iannello, P.U. Foscolo, M. Materazzi, Investigation of single particle devolatilization in fluidized bed reactors by X-ray imaging techniques, Chem. Eng. J. 431 (2022) 133807, https://doi.org/10.1016/j.cej.2021.133807.
[35] R. Solimene, A. Marzocchella, P. Salatino, Hydrodynamic interaction between a coarse gas-emitting particle and a gas fluidized bed of finer solids, Powder Technol. 133 (2003) 79–90, https://doi.org/10.1016/S0032-5910(03)00080-9.
[36] S. Iannello, Z. Bond, A. Sebastiani, M. Errigo, M. Materazzi, Axial segregation behaviour of a reacting biomass particle in fluidized bed reactors: experimental results and model validation, Fuel 338 (2023) 127234, https://doi.org/10.1016/j.fuel.2022.127234.
[37] G. Bruni, R. Solimene, A. Marzocchella, P. Salatino, J.G. Yates, P. Lettieri, M. Fiorentino, Self-segregation of high-volatile fuel particles during devolatilization in a fluidized bed reactor, Powder Technol. 128 (2002) 11–21, https://doi.org/10.1016/S0032-5910(02)00149-3.
[38] J.A. Almendros-Ibáñez, D. Pallarès, F. Johnsson, D. Santana, Voidage distribution around bubbles in a fluidized bed: Influence on throughflow, Powder Technol. 197 (2010) 73–82, https://doi.org/10.1016/j.powtec.2009.08.021.
[39] E. Sette, D. Pallarès, F. Johnsson, Experimental quantification of lateral mixing of fuels in fluid-dynamically down-scaled bubbling fluidized beds, Appl. Energy 136 (2014) 671–681, https://doi.org/10.1016/j.apenergy.2014.09.075.
[40] E. Sette, D. Pallarès, F. Johnsson, Experimental evaluation of lateral mixing of bulk solids in a fluid-dynamically down-scaled bubbling fluidized bed, Powder Technol. 263 (2014) 74–80, https://doi.org/10.1016/j.powtec.2014.04.091.
[41] L. Huilin, H. Yurong, D. Gidaspow, Y. Lidan, Q. Yukun, Size segregation of binary mixture of solids in bubbling fluidized beds, Powder Technol. 134 (2003) 86–97, https://doi.org/10.1016/S0032-5910(03)00126-8.
[42] A. Marzocchella, P. Salatino, V. Di Pastena, L. Lirer, Transient fluidization and segregation of binary mixtures of particles, AICHE J. 46 (2000) 2175–2182, https://doi.org/10.1002/aic.690461110.
[43] S. Qiaoqun, L. Huilin, L. Wentie, H. Yurong, Y. Lidan, D. Gidaspow, Simulation and experiment of segregating/mixing of rice husk-sand mixture in a bubbling fluidized bed, Fuel 84 (2005) 1739–1748, https://doi.org/10.1016/j.fuel.2004.09.026.
[44] M.A. Gilbertson, I. Eames, Segregation patterns in gas-fluidized systems, J. Fluid Mech. 433 (2001) 347–356, https://doi.org/10.1017/S0022112001003950.
[45] A.W. Nienow, D.J. Cheesman, The Effect of Shape on the Mixing and Segregation of Large Particles in a Gas-Fluidised Bed of Small Ones, in: Fluidization, Springer US, Boston, MA, 1980, pp. 373–380, https://doi.org/10.1007/978-1-4684-1045-7_37.
[46] C. Brackmann, M. Aldén, P.E. Bengtsson, K.O. Davidsson, J.B.C. Pettersson, Optical and mass spectrometric study of the pyrolysis gas of wood particles, Appl. Spectrosc. 57 (2003) 216–222, https://doi.org/10.1366/000370203321535141.
[47] A. Elfasakhany, L. Tao, B. Espenas, J. Larfeldt, X.S. Bai, Pulverised wood combustion in a vertical furnace: Experimental and computational analyses, Appl. Energy 112 (2013) 454–464, https://doi.org/10.1016/j.apenergy.2013.04.051.
[48] J.G. Yates, M. MacGillivray, D.J. Cheesman, Coal devolatilisation in fluidised bed combustors, Chem. Eng. Sci. 35 (1980) 2360–2361, https://doi.org/10.1016/0009-2509(80)87019-9.
[49] S. Iannello, D. Macrì, M. Materazzi, A comprehensive assessment of endogenous bubbles properties in fluidized bed reactors via X-ray imaging, Powder Technol. 413 (2023) 118013, https://doi.org/10.1016/j.powtec.2022.118013.
[50] Z. Yang, L. Duan, L. Li, D. Liu, C. Zhao, Movement and mixing behavior of a single biomass particle during combustion in a hot fluidized bed combustor, Powder Technol. 370 (2020) 88–95, https://doi.org/10.1016/j.powtec.2020.05.037.
[51] A. Köhler, D. Pallarès, F. Johnsson, Modeling Axial Mixing of fuel Particles in the Dense Region of a Fluidized Bed, Energy Fuel 34 (2020) 3294–3304, https://doi.org/10.1021/acs.energyfuels.9b04194.
[52] L.R. Glicksman, M.R. Hyre, P.A. Farrell, Dynamic similarity in fluidization, Int. J. Multiphase Flow 20 (1994) 331–386, https://doi.org/10.1016/0301-9322(94)90077-9.
[53] E. Sette, D. Pallarès, F. Johnsson, F. Ahrentorp, A. Ericsson, C. Johansson, Magnetic tracer-particle tracking in a fluid dynamically down-scaled bubbling fluidized bed, Fuel Process. Technol. 138 (2015) 368–377, https://doi.org/10.1016/j.fuproc.2015.06.016.
[54] N. Jand, P.U. Foscolo, Decomposition of wood particles in fluidized beds, Ind. Eng. Chem. Res. 44 (2005) 5079–5089, https://doi.org/10.1021/ie040170a.
[55] A. Einstein, Investigations on the Theory of the Brownian Movement, Courier Corporation, 1956.
[56] D.C. Guío-Pérez, F. Johnsson, D. Pallarès, Experimental investigation of the lateral mixing of large and light particles immersed in a fluidized bed, Fuel 346 (2023) 128343, https://doi.org/10.1016/j.fuel.2023.128343.
[57] K.G. Palappan, P.S.T. Sai, Studies on segregation of binary mixture of solids in a continuous fast fluidized bed. Part I. Effect of particle density, Chem. Eng. J. 138 (2008) 358–366, https://doi.org/10.1016/j.cej.2007.06.008.
[58] J.M. Beeckmans, J. Nllsson, J.F. Large1, Observations on the mechanisms of segregation in flotsam-rich, fully fluidized beds, Ind. Eng. Chem. Fundam. 24 (1985) 90–95, https://doi.org/10.1021/i100017a015.
[59] J. Chladek, C.K. Jayarathna, B.M.E. Moldestad, L.A. Tokheim, Fluidized bed classification of particles of different size and density, Chem. Eng. Sci. 177 (2018) 151–162, https://doi.org/10.1016/j.ces.2017.11.042.
[60] B. Formisani, R. Girimonte, T. Longo, The fluidization pattern of density-segregating binary mixtures, Chem. Eng. Res. Des. 86 (2008) 344–348, https://doi.org/10.1016/j.cherd.2007.11.004.
[61] S. Du, L. Zhao, X. Chen, B. Yang, Q. Zhou, Effect of Stefan flow on the drag force of single reactive particle surrounded by a sea of inert particles, Chem. Eng. Sci. 253 (2022) 117546, https://doi.org/10.1016/j.ces.2022.117546.
[62] M. Fiorentino, A. Marzocchella, P. Salatino, Segregation of fuel particles and volatile matter during devolatilization in a fluidized bed reactor—I. Model development, Chem. Eng. Sci. 52 (1997) 1893–1908, https://doi.org/10.1016/S0009-2509(97)00018-3.
[63] A. Köhler, E. Cano-Pleite, A. Soria-Verdugo, D. Pallarès, F. Johnsson, Modeling the motion of fuel particles in a fluidized bed, Fuel 305 (2021), https://doi.org/10.1016/j.fuel.2021.121424.
[64] R. Kurose, H. Makino, S. Komori, M. Nakamura, F. Akamatsu, M. Katsuki, Effects of outflow from the surface of a sphere on drag, shear lift, and scalar diffusion, Phys. Fluids 15 (2003) 2338–2351, https://doi.org/10.1063/1.1591770.
[65] S. Du, Y. Zhao, Q. Zhou, Impact of Stefan flow on drying performance in fluidized beds: a coarse-grained CFD-DEM study, Powder Technol. 469 (2026) 121840, https://doi.org/10.1016/j.powtec.2025.121840.